crystals

MDPI

Article

Simulation of Surface Segregation in Nanoparticles of Pt-Pd Alloys

Jose Brito Correia * and Ana Isabel de Sá

LNEG, Laboratório Nacional de Energia e Geologia, Estrada do Paço do Lumiar, 1649-038 Lisboa, Portugal; ana.sa@lneg.pt

* Correspondence: brito.correia@lneg.pt; Tel.: +351-21-0924600

Abstract: Platinum (Pt) and palladium (Pd) are crucial in hydrogen energy technologies, especially in fuel cells, due to their high catalytic activity and chemical stability. Pt-Pd nanoparticles, produced through various methods, enhance catalytic performance based on their size, shape, and composition. These nanocatalysts excel in direct methanol fuel cells (DMFCs) and direct ethanol fuel cells (DEFCs) by promoting alcohol oxidation and reducing CO poisoning. Pt-Pd catalysts are also being explored for their oxygen reduction reaction (ORR) on the cathodic side of fuel cells, showing higher activity and stability than pure platinum. Molecular dynamics (MD) simulations have been conducted to understand the structural and surface energy effects of PdPt nanoparticles, revealing phase separation and chemical ordering, which are critical for optimizing these catalysts. Pd migration to the surface layer in Pt-Pd alloys minimizes the overall potential energy through the formation of Pd surface monolayers and Pt-Pd bonds, leading to a lower surface energy for intermediate compositions compared to that of the pure elements. The potential energy, calculated from MD simulations, increases with a decreasing particle size due to surface creation, indicating higher reactivity for smaller particles. A general contraction of the average distance to the nearest neighbour atoms was determined for the top surface layers within the nanoparticles. This research highlights the significant impact of Pd segregation on the structural and surface energy properties of Pt-Pd nanoparticles. The formation of Pd monolayers and the resulting core–shell structures influence the catalytic activity and stability of these nanoparticles, with smaller particles exhibiting higher surface energy and reactivity. These findings provide insights into the design and optimization of Pt-Pd nanocatalysts for various applications.

Keywords: molecular dynamics; Pt-Pd alloys; nanoparticles; catalysis

Academic Editor: Balázs Zsirka

Received: 5 December 2024
Revised: 18 December 2024
Accepted: 22 December 2024
Published: 7 January 2025

Citation: Correia, J.B.; de Sá, A.I. Simulation of Surface Segregation in Nanoparticles of Pt-Pd Alloys. *Crystals* **2025**, *15*, 53. https://doi.org/10.3390/cryst15010053

1. Introduction

Platinum and palladium are among the catalytic materials most applied in different hydrogen energy technologies, particularly in fuel cells for chemical energy conversion to electricity [1–10]. Both metals have high catalytic activity [10] and high chemical stability, with a consequent resistance to corrosion phenomena [11]. In heterogeneous catalysis, a larger surface area is essential for obtaining higher reaction conversion while using a minimum catalyst amount, and this can be achieved using nanoparticles. Nanoparticles can be produced by different methods, from physical to chemical synthesis [12], and the correspondent catalytic activity depends on the size, shape, structure, composition, and substrate, along with other effects occurring during catalytic action such as poisoning, particle modification, and dissolution.

In fuel cells, Pt-Pd-alloyed nanocatalysts have been showing good performance at the anodic side of direct methanol fuel cells (DMFCs) and direct ethanol fuel cells (DEFCs) by promoting alcohol oxidation and decreasing the CO adsorption, which causes catalyst poisoning [4,13–15]. For example, Antolini notes that the presence of palladium up to 33% lessens the probability of having three atomic platinum sites close enough to promote the formation of strongly bound intermediary compounds, and this feature changes the kinetics of the reaction and decreases the poisoning effect [4]. Yang et al. reported data for the MOR (methanol oxidation reaction) from a Pt-Pd porous nanocatalyst and explained that the higher activity might be related to an increase in the plane ratio l(111)/l((200) when exposed to the electrolyte, compared with a commercial platinum catalyst and standards [13]. This feature is in agreement with a recently reported theoretical study demonstrating that the PtPd(111) planes are better able to promote OH absorption, which is a fundamental intermediary stage necessary for methanol oxidation and the removal of absorbed CO [14]. On the other hand, Zhang et al. studied the methanol oxidation activity in a series of catalysts, from a low to high content in palladium, and found that the highest value was obtained for the catalyst $Pt_{25}Pd_{75.}$ These catalyst nanoparticles have a particle diameter size of around 2.3 nm and are agglomerated in nanoporous clusters with a diameter between 50 and 100 nm, with preferential growth of the (111) planes. The catalysts were prepared by a chemical reduction method followed by impregnation in carbon particles and showed a sawtooth-like structure characterized by a high number of twinning boundaries [15]. Another relevant effect promoted by palladium is tolerance to methanol and ethanol crossover from the anodic to the cathodic side, which is a harmful feature that affects the performance of DMFCs or DEFCs [16,17].

The Pt-Pd nanocatalysts have also been examined for their ability to replace the platinum catalysts for the ORR (oxygen reduction reaction) in the cathodic side of fuel cells [16–21]. Li et al. reported that a catalyst with a Pt_3Pd_1/C composition has higher oxygen reduction activity than a platinum catalyst prepared through the same synthesis method and with a similar metal content [18]. However, the more reported effect of replacing part of the platinum metal content with palladium is the increase in stability, and this is reflected in a lower decrease in the electrochemical active surface area and better energy performance in long-term durability tests [18–20]. Most of the reported studies on Pt-Pd catalysts are about catalysts synthesized at room temperature with nanoparticles with low Miller index planes, where the Pt(111) plane is prominent, followed at a much lower extent by Pt(200), Pt(220), and Pt(311). However, it is also well known that higher index planes promote higher catalytic activity due to a higher density of atomic steps, ledges, and kinks, which are preferential sites for chemical bond breaking [22–25].

More recent reports include studies of more sophisticated carbon substrates such as multi-walled carbon nanotubes, carbon nanofibers, porous carbon substrates or reduced graphene oxide [26–30], and in situ fuel cell tests [31], which evidence the relevance of these catalysts.

In order to understand the structure and the surface energy effects of Pd-Pt nanoparticle catalysts, several Pd-Pt nanoparticles with three different compositions and sizes were simulated using molecular dynamics (MD). Molecular dynamics is a simulation technique for computing the equilibrium and transport properties of a classical many-body system, where each atom is assumed as a point mass, and the atomic motion is based on Newton's equations. To describe the interactions in the Pt-Pd alloy, an embedded atom method (EAM) potential was used. This type of potential is extensively used for metals [32]. This type of potential is non-pairwise in the sense that it is based on concepts from density functional theory, which stipulate, in general, that the energy of a solid is a unique function of the electron density and thus correlates well with more precise bonding methods.

The LAMMPS software [33] from Sandia Labs is extensively used to perform MD simulations in materials using an EAM potential, as well as simulate X-ray diffraction patterns from atomistic simulation results [34]. The accessed phase diagram for Pt-Pd [35] indicates phase separation into two face-centred cubic (fcc) structures below 770 °C. Several attempts have been made to simulate the structure of PdPt [36–39] using EAM. In ref [37], the possibility of ordered structures was considered; recently, more accurate methods [39] have identified chemical ordering in the form of Pd channels in Pt, which were detected experimentally [40]. The structure and composition of the top layers of Pt-Pd nanoparticles are critical for optimizing these catalysts. Simulations using a range of particle sizes and compositions elucidate the segregation and relaxation mechanisms acting at the surface.

2. Experimental Details

The simulation of nanoparticles of several Pt-Pd alloys was launched with a face-centred cubic (fcc) lattice and three particle sizes, consisting of 4^3, 6^3 and 8^3 unit cells, constituted by 256, 864, and 2048 atoms, respectively. These sets were simulated using canonical ensemble (NVT) with a timestep of 1 femtosecond and non-periodic and shrink-wrapped boundary conditions in three dimensions. In Table 1, the compositions used are presented. A canonical ensemble with 4000 atoms (10^3 fcc cells) and periodic boundary conditions in all directions was used to simulate the potential energy of the respective bulk alloys. Additionally, for the simulation of surface properties in flat surfaces, we used the canonical ensemble (NVT) and non-periodic and with shrink-wrapped boundary conditions in one dimension, while in the other two directions, periodic boundary conditions were used, simulating an infinite flat surface. The OVITO software (version 3.10.6) was used for processing results [41].

Table 1. Atomic percentage of each element in the particles.

Designation	Pd100	Pt19Pd81	Pt50Pd50	Pt86Pd14	Pt100
Pt (at.%)	0	19	50	86	100
Pd (at.%)	100	81	50	14	0

The software LAMMPS (version of 17 April 2024) of Sandia Labs [42,43] was used for (a) molecular dynamics (MD) and (b) simulated X-ray diffraction of MD-simulated materials. In order to simulate an equilibrium structure, the typical sequence of MD simulation involved several steps of energy minimization of the initial configuration at 2000 K for 1×10^5 time steps, cooling to the final simulation temperature, 300 K, for a period of 6×10^6 time steps and energy minimization at a constant temperature of 300 K for an additional period of 6×10^6 time steps. Starting the simulation from a high temperature ensured enough atomic mobility for the development of equilibrium structures so that the present simulations are representative of alloy structures obtained experimentally after annealing.

The EAM potential for Pt-Pd was retrieved from NIST [44] referring to the original work of Zhou [45]. The same procedure, using the same data set for the simulation of a binary alloy, was previously reported in the literature [46,47].

3. Results

The external shape of the nanoparticles is approximately spherical, as shown in Figure 1. However, the particles with a higher content of Pd tend to present a faceted surface with compact planes at the top, whereas the alloy with high Pt content shows a much smoother surface corresponding to high index crystalline planes.

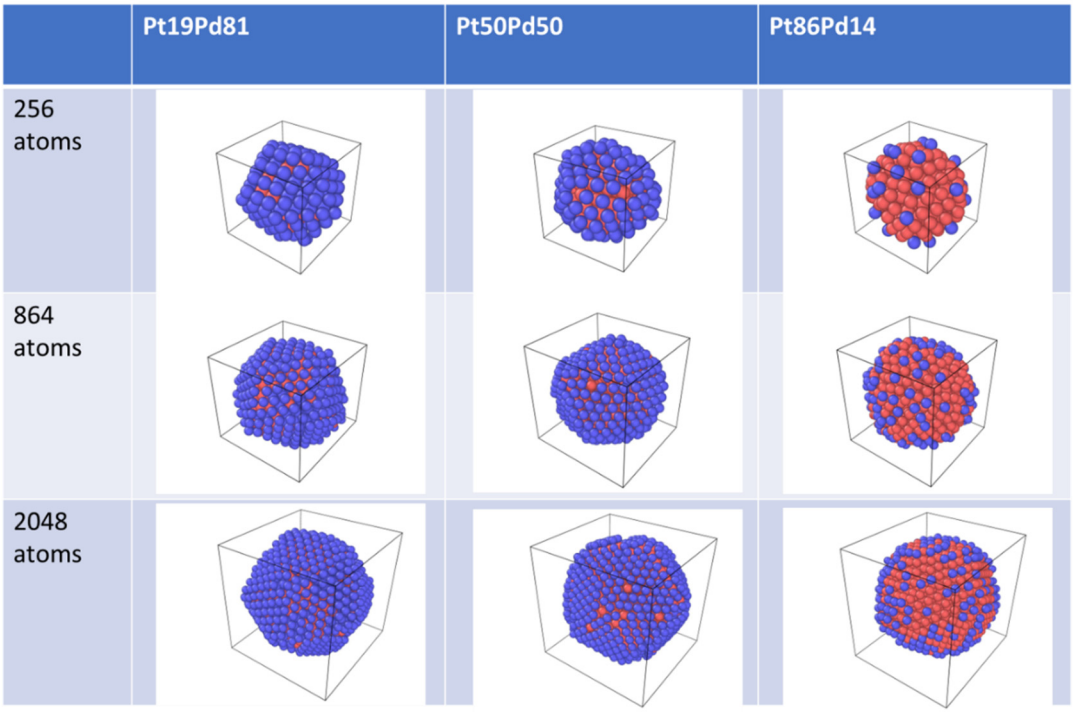

Figure 1. Equilibrium external shape of the nanoparticles, Pt, red; Pd, blue.

The cross-section of particles is depicted in Figure 2. It can be seen that there is an enrichment in Pd of the outermost layer of the particles for the complete range of compositions and dimensions.

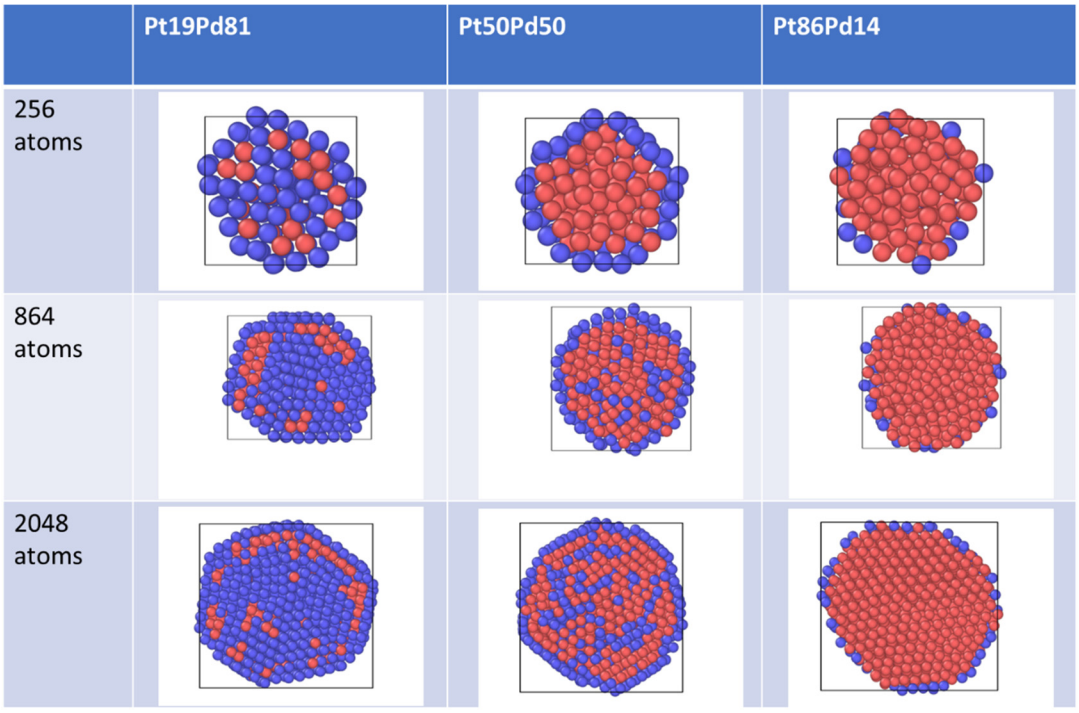

Figure 2. Cross-section through the centre of the nanoparticles. Pt, red; Pd, blue.

The MD simulation results in the formation of a Pd monolayer up to 50%Pd composition and a clear enrichment in Pd even in the high Pt alloy (Pt86Pd14) are shown in Figures 1 and 2.

The radial distribution of elements in the larger particles (with 2048 atoms) can be seen in Figure 3 and evidences the segregation of Pd to the surface for all compositions. For Pt19Pd81 and Pt50Pd50, a Pd monolayer is formed at the surface, whereas underneath this monolayer, a Pt-rich layer is present, conversely corresponding to a Pd-depleted zone. For the high Pt composition (Pt86Pd14), the Pd content is almost exclusively concentrated near the surface of the nanoparticle.

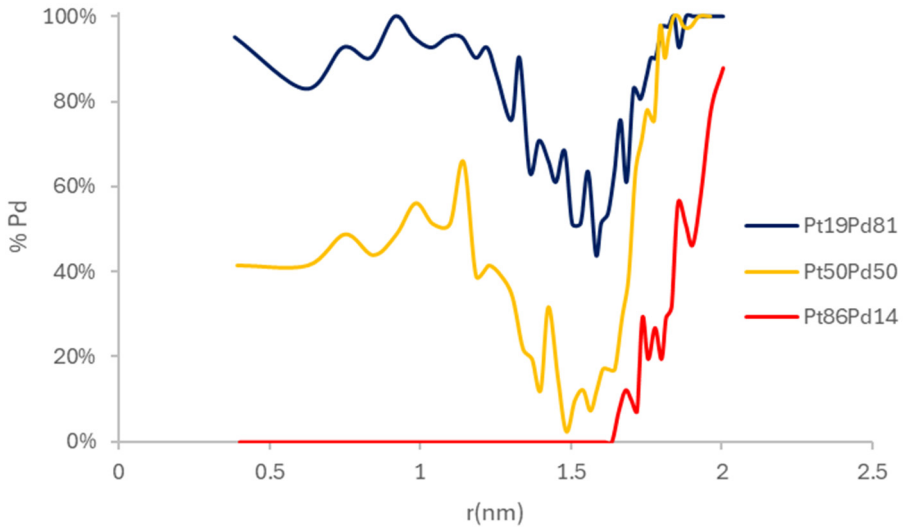

Figure 3. Radial distribution of elements in particles with 2048 atoms.

The surface segregation of Pd is a size-independent feature in the Pt-Pd alloys. A flat surface simulation involving 32,000 atoms of a Pt50Pd50 alloy again shows this feature, as shown in Figure 4.

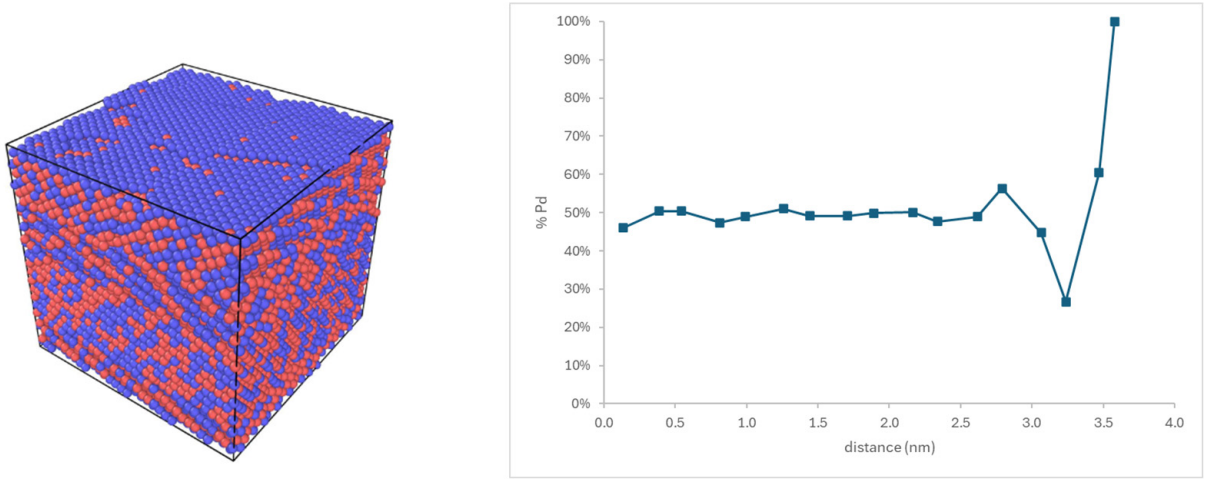

(**a**) (**b**)

Figure 4. (**a**) Equilibrium free surface of Pt50Pd50 alloy; Pt, red; Pd, blue; (**b**) composition versus distance evidencing surface segregation of Pd.

The internal structure of the nanoparticles, after removal of the top surface layer, is shown in Figure 5. This structure characterization was obtained in the OVITO software using the "common neighbour analysis" modification and eliminating the top atomic layer.

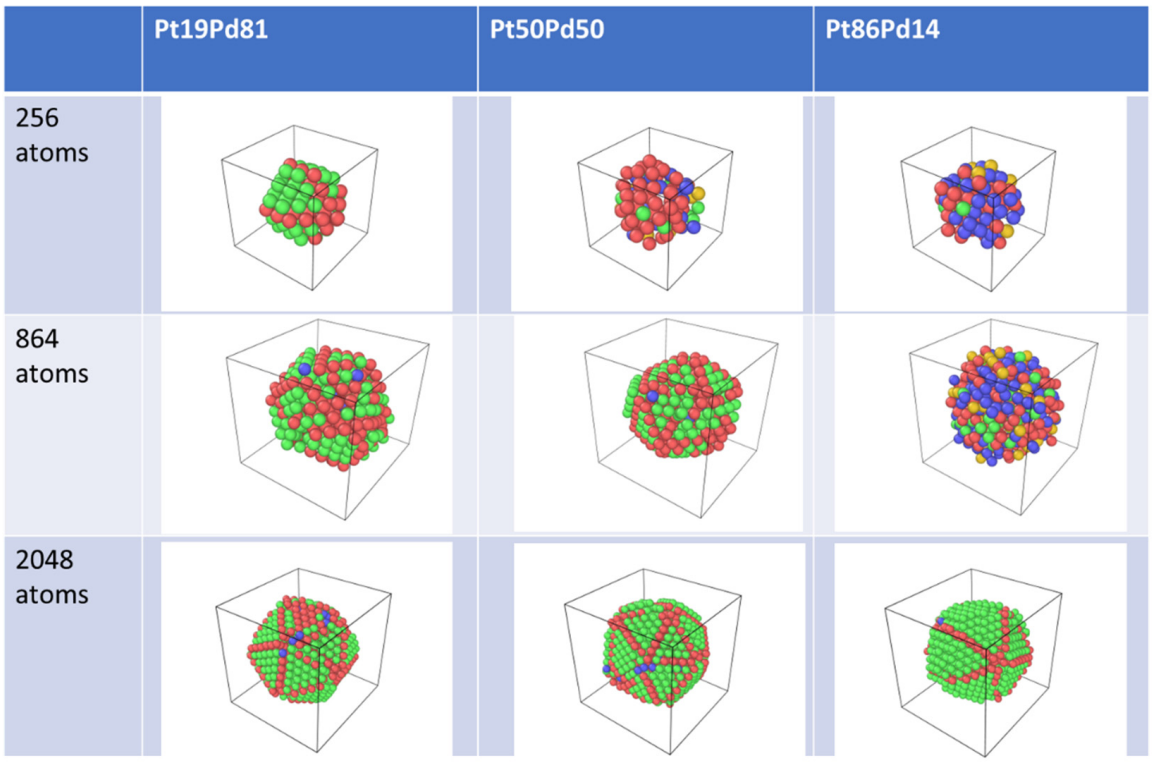

Figure 5. Internal crystal structure of the nanoparticles; green—fcc; red—hcp; blue—bcc.

The internal crystal structure of the nanoparticles is predominantly of the fcc type, with grains separated by planer defects, as shown in Figure 5. The exception is the smallest of the nanoparticles with the highest Pt concentration; in this case, the structure is highly disordered.

The simulated X-ray diffraction patterns for the Pd-rich alloy particles (Pt19Pd81) that are well crystalized throughout the entire size range are shown in Figure 6. The peaks correspond to those of Pd, albeit very broad, especially for the smallest particles, as is typical for nanoparticles.

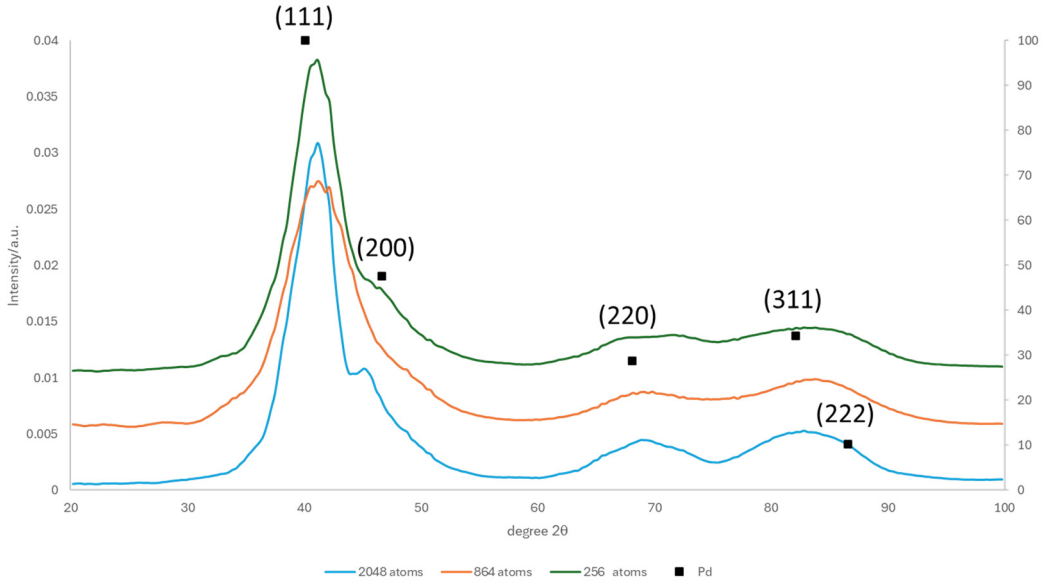

Figure 6. Simulated X-ray diffraction patterns using Cu radiation for Pt19Pd81 alloy particles together with typical diffraction positions and intensities for pure Pd.

The change in potential energy owing to the creation of surfaces is

$$\Delta Ep = Ep_{surface} - Ep_{bulk}$$

where $Ep_{surface}$ is obtained from a simulation with non-periodic and shrink-wrapped boundaries in three directions (sss), and Ep_{bulk} is obtained from periodic boundaries in three directions (ppp, representing the bulk material properties). In the case of the flat surface simulation, pps boundaries were used. In Figure 7, MD simulations with canonical ensembles (NVT) versus composition and size are depicted. A clear increment of potential energy with diminishing size of the particles is obtained for all compositions. This indicates the smaller particles are in a higher energy state and therefore are more reactive. A similar trend is depicted in Figure 8 relative to the surface energy of the nanoparticles. The surface area was calculated assuming a spherical particle, and for its radius, an average over the three-simulation axis was considered. The cohesive energy of platinum is larger than that of palladium; therefore, a continuous increase in the potential energy per atom or in the surface energy would be expected for the various compositions ranging from pure Pd to pure Pt. In contrast, the potential energy values (Figure 7) and the surface energy (Figure 8) are proximately constant up to 50% platinum composition, reflecting the formation of a continuous layer of Pd at the surface of the particles up to that composition, imparting to the material properties similar those of pure Pd. It should also be noted that while the high Pt content alloy (Pt86Pd14) has a very disordered structure, especially for the smallest nanoparticles, as shown in Figure 5, both pure Pt and Pd particles in the whole size range have a fully crystalline fcc structure.

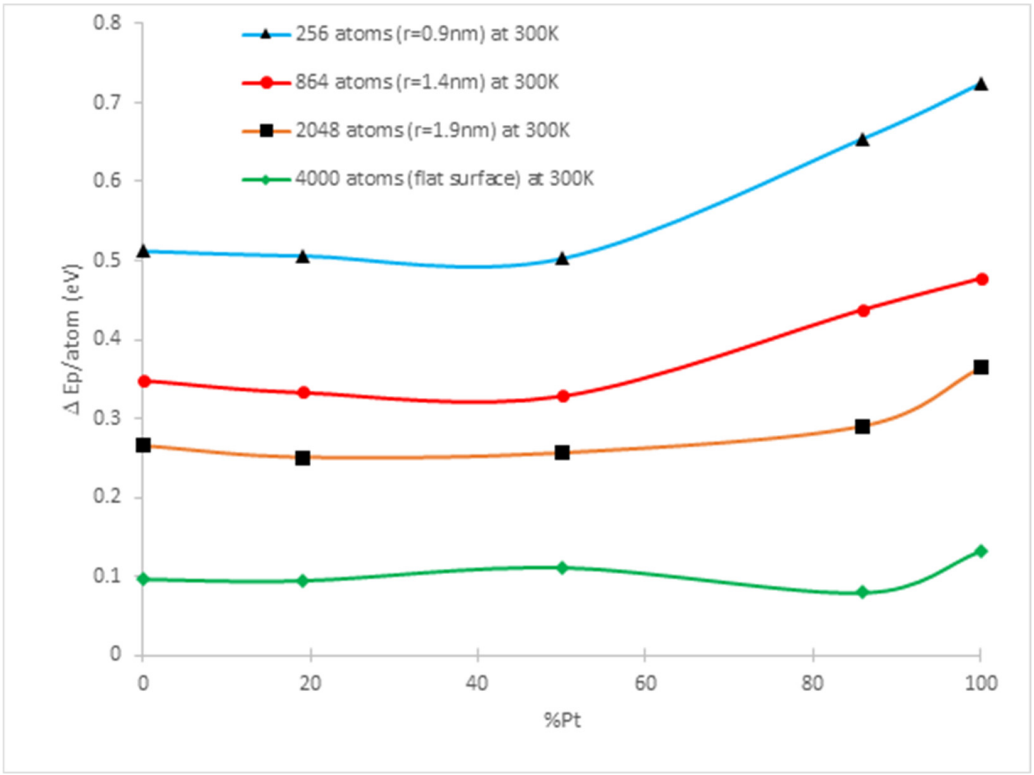

Figure 7. Potential energy gain versus bulk alloy for the different compositions and sizes obtained from the MD simulation.

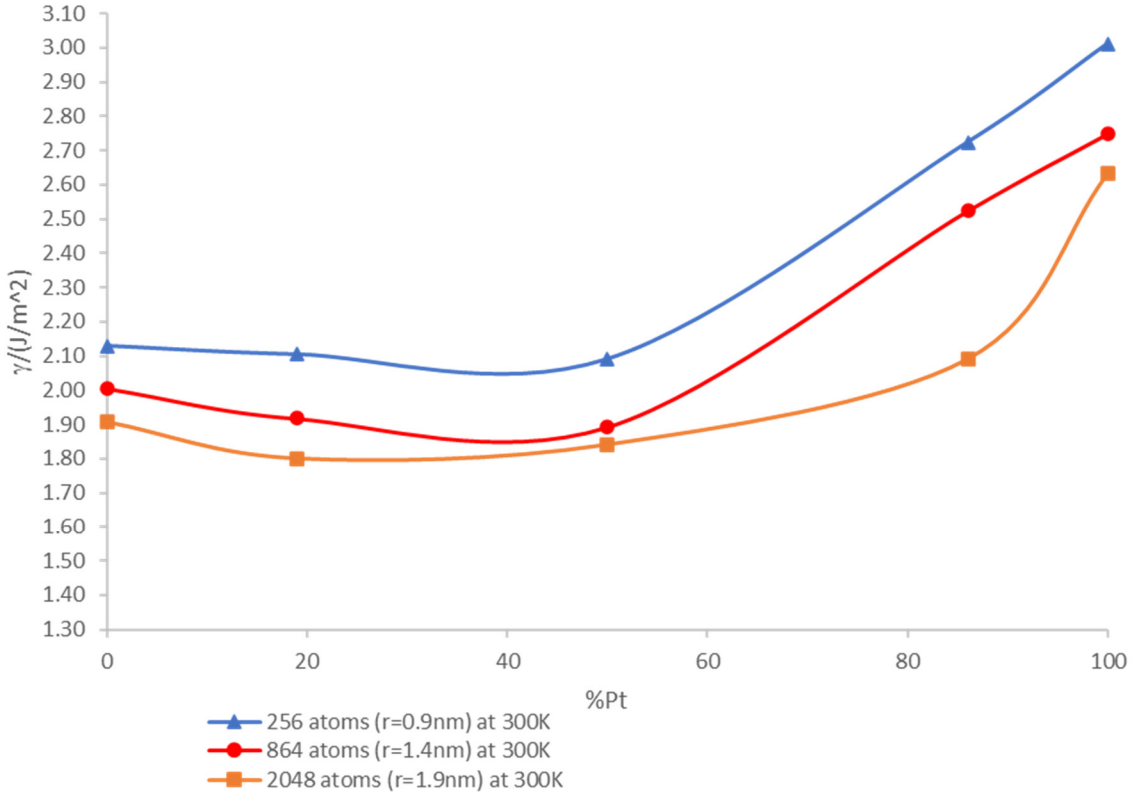

Figure 8. Surface energy versus composition and size obtained from the MD simulations.

The simulation results were further analyzed in terms of the average distance to first near neighbour atoms, <dNN>, within selected sets of atoms:

$$\langle \mathrm{dNN} \rangle = 1/n \sum_{i=1}^{n} \mathrm{dNN};\ \mathrm{dNN} < 0.3\ \mathrm{nm}$$

The limit of 3 was set considering the dNN of both Pt and Pd fcc structures (0.27748–0.27511 nm, respectively) to capture only the nearest neighbour bonds typical of the fcc structure.

Five sets of atoms were considered:

- 1-<dNN> within the first atomic layer (top) of the surface;
- 1,2-<dNN> between the first and second atomic layers;
- 2-<dNN> within the second atomic layer from the surface;
- 2,3-<dNN> between the second and atomic layers;
- 3-<dNN> within the third atomic layer from the surface.

Extraction of the individual layers was performed with the OVITO software using the modification "polyhedral template matching". The results obtained for the variation in the average dNN in the five sets considered relative to those of the perfect fcc lattice <dL> are shown in Figure 9a for the particle simulations with 2048 atoms (sss boundaries) and Figure 9b for the flat surface simulation with 4000 atoms (pps boundaries). The variation in the average dNN, generally a contraction, is normalized to those of the perfect fcc lattice <dL> of the alloy. For the alloys, the Vegard law, i.e., a linear combination of the lattice parameters of the pure elements, is assumed.

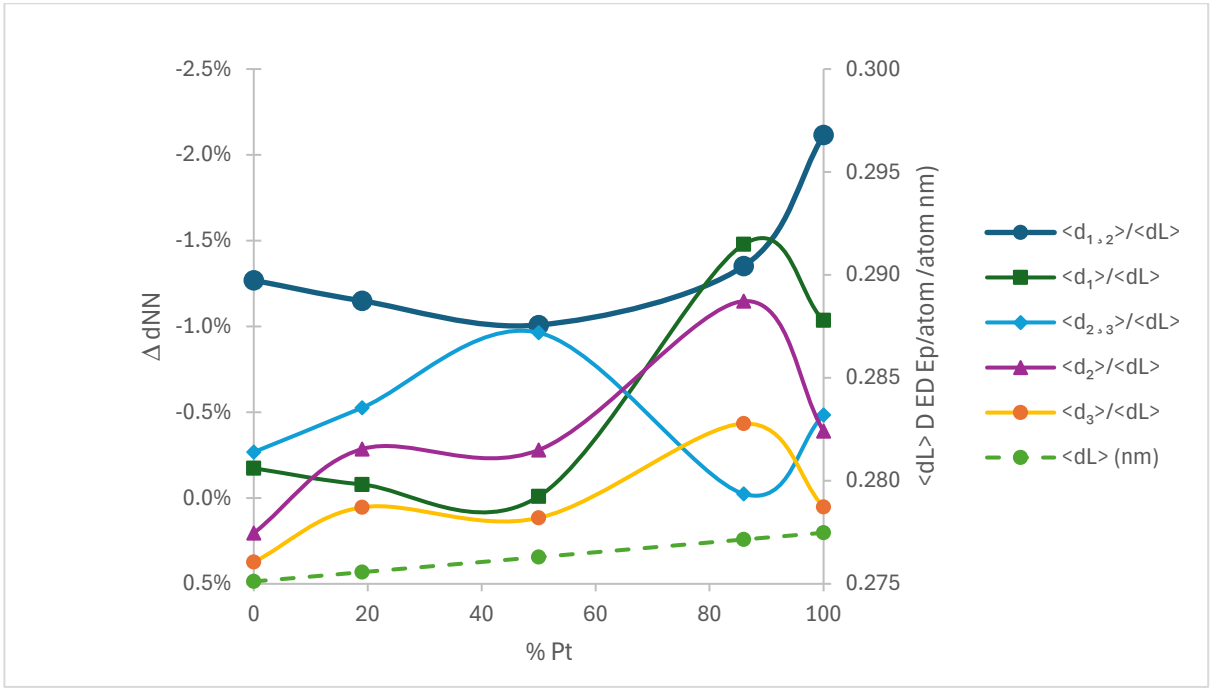

(**a**)

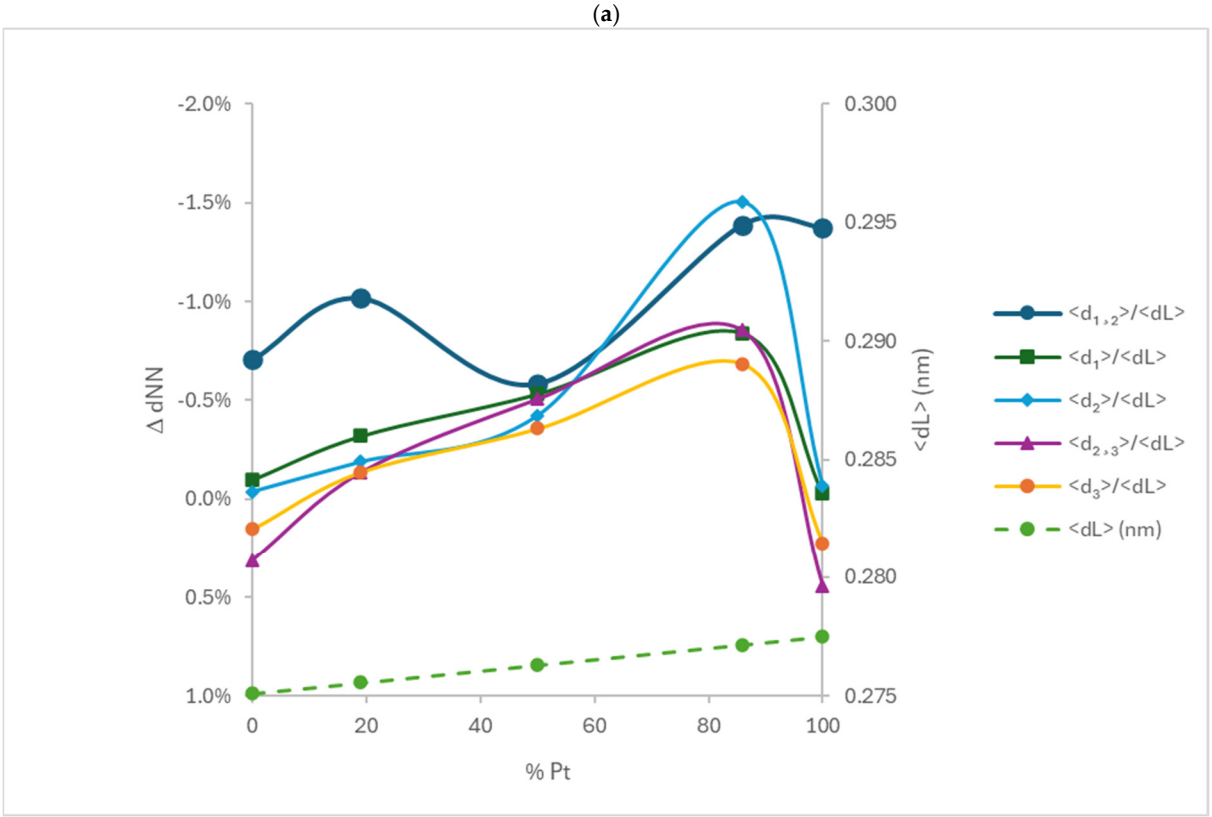

(**b**)

Figure 9. Variation in the average dNN in the five sets considered relative to those of the perfect fcc lattice: (**a**) simulations of spherical particles with 2048 atoms and (**b**) simulation with 4000 atoms and flat surface.

4. Discussion

Most of the electrocatalysts are usually obtained in a variety of carbon supports and by electroreduction processes requiring surfactants and capping agents to control nanoparticle growth and shape, which have a direct influence on the catalytic activity. These chemical

methods can be tailored for forming core–shell structures, which might have similarities to the structures obtained in this work. Furthermore, heat treatments to minimize possible chemical contaminations from the reduction processes are often necessary, and that can change the initial nanoparticle structures [48,49], achieving more thermodynamic stable structures similar to those reported in this research. The predicted evolution of core–shell Pd@Pt structures on heating to high temperature is complete Pt-Pd alloying and intense Pd migration to the surface after melting [50].

A report on Pt-Pd alloys using similar atomistic methods to those of present research predicts surface segregation of Pd, which diminishes with the nanoparticle size and with increasing temperature [47]. Similar results were obtained with Monte Carlo Simulation [51]. The Pd segregation was also detected experimentally in Pt-Pd alloys [52]. A density functional theory (DFT) study of Pt-Pd nanoparticles has shown that the stability of the nanoparticles is strongly associated with surface contraction [53]. This ab initio simulation procedure is more precise than the use of AEM potentials and gives realistic indications of the outcome in this system. In the present research, the contraction between the first and second atomic layers $<d_{1,2}>/<dL>$ versus composition in Figure 9a correlates well with the variation in surface energy versus composition, Figure 8. The surface energy is roughly proportional to the number of nearest neighbours, which are removed when the surface is created [54].

All the nanoparticles show segregation of palladium atoms to the surface, and consequently, the corresponding core is enriched in platinum atoms (Figures 1–3). This feature promotes the formation of a core–shell structure, which is clearly visible for the Pd50Pt50 particles, where a complete surface monolayer of palladium atoms is formed. The main factors affecting the surface segregation in bimetallic nanoparticles are related to the relative bond strengths of the metal components (A–A, B–B, and A–B), the surface energy, atomic size (Wigner–Seitz radius), and charge/electronic effects for extra-small particle sizes (number of atoms less than 50) [47,55,56]. For the Pd-Pt nanoparticles, the segregation of palladium to the surface is mainly associated with the higher cohesive energy of platinum and lower surface energy of palladium [47,55,56] since the atomic radii are similar [55]. The data of the particle surface energies calculated in this work show an increase in this parameter with the increase of platinum content and a decrease in particle size (Figure 8). Since palladium is segregated to the surface layers, the lower energy is associated with the predominant presence of this element at the surface. For the same composition, the FCC lattice parameter also calculated in this research for the particle with 864 and 2048 atoms decreases directly with the particle size, which is according to the tendency reported for the FCC lattice nanoparticles [57–59].

The surface energy (Jm^{-2}) is generally inversely related to the atomic density of the crystal surface planes: denser surfaces show lower surface energies because it is necessary to break fewer bonds between the dense planes. As a rule, surfaces of higher energy have higher catalytic activity [60]. The most common crystalline planes of platinum and palladium have surface energies around 1–2 Jm^{-2} [61,62], whereas the data obtained in this work are slightly higher, in the range of 1.8–2.9 Jm^{-2}, which is associated with the nano size of the particles.

Another interesting feature observed, especially in the Pt19Pd81 particles, independent of the particle size, is a second intermediary layer enriched in platinum atoms immediately below the surface layer (Figures 2 and 4). This effect seems to have a tendency to form a three-shell onion-like structure (A-B-A) and has been found on various bimetallic nanoalloys such as PdAg or PdAu (Pd = B element), but also in PtPd clusters (Pt = B element,) where this specific configuration contributes to the particle stabilization [63–65].

The distorted fcc structure, as for the smaller size particles of Pt86Pd14 in Figure 5, is also a relevant outcome since the electrocatalysis activity is directly related to the strain and electronic structure of the surface atoms [66–68]. The electrocatalysts with strain-rich surfaces (SREs) promote changes in the adsorption (desorption) and in the splitting ability of the chemical species (H_2, O_2, OH^- or H_2O) involved in the reactions, which can contribute to an increase in the global chemical conversion rates. This feature is more evident in bimetallic catalysts with complex nanostructures (core–shell, nanocages, etc.) [69]. However, crystalline defects, such as vacancies, dislocations or voids, can also promote strain changes and increase the catalytic performance [67].

The characteristics of the potentials used in the simulation are decisive for the final simulation result. Therefore, it was obtained from the NIST database [44] that the variation in potential energy vs. interatomic spacing, r, for an fcc structure, was generated based on the ideal atomic positions without relaxing the system. The plots of potential energy vs. interatomic spacing for the Three possible interactions are shown in Figure 10.

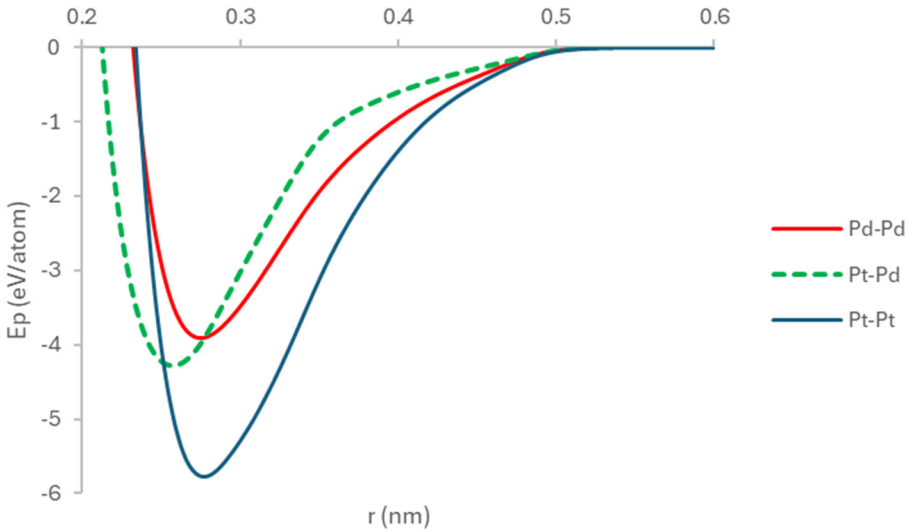

Figure 10. Potential energy versus interatomic position for ideal fcc structure without relaxation.

The minimum in the curves of Figure 10, corresponding to the lowest possible energy and to the respective equilibrium distance of the first near neighbour (NN), are slightly different depending on the type of bond. The equilibrium Pt-Pd bond has a shorter NN length than those of either Pt-Pt or Pd-Pd, hence enabling the accommodation of surface contraction.

The effect of increased surface curvature as the particles became smaller is very clear, from Figures 8 and 9. The smaller nanoparticles have higher surface energy values for the whole composition range. Similar molecular dynamics studies of Au and Fe indicate conversely that surface energy decreases with the increasing of nanoparticle size, with results comparable to the experimental values [70,71]. The increase in surface energy for smaller nanoparticles is attributed to the larger fraction of the surface, namely edge and corner atoms, where there are more under-coordinated atoms and therefore, higher surface energy [71]. With the EAM interatomic potential, it has been identified the effect of surface contraction in nanoparticles, i.e., smaller NN distances especially between the first and second layers near the surface. The Pd migration to the surface layer in Pt-Pd alloys enables minimizing the overall potential energy of the ensemble through the formation of top Pd monolayers and Pt-Pd bonds accommodating smaller $<d_{1,2}>$ distances. In alloys with very low content of Pd, this is not possible and $<d_{1,2}>$ distances much smaller than the minimum of the Ep vs. r (Figure 10), a maximum contraction of about 2% in $<d_{1,2}>$ is seen in Figure 9a)

for pure Pt. This contraction imposed on the Pt-Pt bonds of atoms close to the surface leads to higher surface energy values. In contrast, the formation of a Pd surface monolayer for the Pt50Pd50 composition, Figure 2 and the ensuing accommodation in $<d_{1,2}>$ through the Pt-Pd bond gives rise to minima in Figure 9 for the Pt50Pd50 composition. Similarly, the surface energy determined for intermediate compositions, Figure 8, is smaller than that of the pure terminal elements.

The nanoparticle structures obtained in this work for the compositions Pt19Pd81 and Pt50Pd50 show a complete layer of palladium formed at the surface, which corresponds to a core shell structure: PtPd@Pd. Core–shell structures (Pt@Pd) have been obtained experimentally and show good results for methanol oxidation reaction (MOR) in acid media (anode side) [72]. Experimental evidence of Pd segregation in Pt-Pd nanoparticles has been detected after exposure at high temperatures (processing or annealing at 488–573 K) [73,74]. Using Ambient Pressure XPS (APXPS) associated with a synchrotron, it was possible to obtain non-destructive depth profiles of composition in Pt50Pd50 bimetallic nanoparticles with a diameter of 15 nm, synthesized using colloidal chemistry methods. These nanoparticles have a core–shell structure with the shell significantly Pd-rich, 84%Pd at a depth of 0.7 nm, converging to the average composition, to 52%Pd, 1.6 nm below the surface [73]. Nanoparticles with 5 nm in diameter of Pt70Pd30 were subjected to thermal treatment at 300 °C and subsequently to XPS measurements. The results indicate that a core–shell structure with a Pd-enriched shell and a Pt-rich core is formed [74].

The structure of the particles for the composition Pt86Pd14, where both metals are present at the nanoparticle surface, might have application for ORR in PEMFCs (cathodic side, acid media), since the palladium increases activity and long-term stability, as it was found by Li et al. for an alloy composition close to that of the present research: (Pt3Pd/C) [18].

5. Conclusions

Molecular dynamics simulations representative of equilibrium structures show the formation of a Pd surface monolayer or significant Pd enrichment in Pt-Pd alloys. Pd is present in the outermost layer of Pt-Pd nanoparticles across all compositions and sizes. Pt-Pd nanoparticles are approximately spherical, with higher Pd content alloys showing faceted low-index plane surfaces. The radial distribution data confirm Pd segregation to the surface for all compositions, with a Pd monolayer forming at the surface and a Pt-rich layer beneath it. Simulated X-ray diffraction patterns for Pd-rich alloy particles show broad peaks typical of nanoparticles, indicating higher reactivity for smaller particles. The Pd migration to the surface layer in Pt-Pd alloys minimizes the overall potential energy through the formation of Pd surface monolayers and Pt-Pd bonds, leading to lower surface energy for intermediate compositions compared to that of pure elements. The contraction between the first and second atomic layers at the surface is the main driver of the variation in surface energy versus composition. The surface energy values and predicted structures are consistent with those reported in the literature, validating the present simulation framework.

Pd segregation significantly impacts the structural and surface energy properties of Pt-Pd nanoparticles, influencing catalytic activity and stability. The results of this work are a relevant contribution to the future design of Pd-Pt nanocatalysts regarding the particle size, palladium content, structure, surface segregation of elements and surface energy, which have been considered key factors for catalytic activity.

Author Contributions: Conceptualization, J.B.C. and A.I.d.S.; Methodology, J.B.C. and A.I.d.S.; Software, J.B.C.; Writing—review & editing, J.B.C. and A.I.d.S. All authors have read and agreed to the published version of the manuscript.

Funding: LNEG, Laboratório Nacional de Energia e Geologia, Portugal.

Data Availability Statement: Data is contained within the article.

Acknowledgments: The support of Doutora Ana Estanqueiro of LNEG for the use of computer facilities is deeply acknowledged. The assistance of Eng. Paulo Luz and Doutor António Couto in software installation is also very much acknowledged.

Conflicts of Interest: The authors declare no conflict of interest.

References

1. Zhang, J. *PEM Fuel Cell Electrocatalysts and Catalyst Layers: Fundamentals and Applications*; Springer Nature: Dordrecht, The Netherlands, 2008. [CrossRef]
2. Ganesan, A.; Narayanasamy, M. Ultra-low loading of platinum in proton exchange membrane-based fuel cells: A brief review. *Mater. Renew. Sustain. Energy* **2019**, *8*, 18. [CrossRef]
3. Shao, M.; Chang, Q.; Dodelet, J.P.; Chenitz, R. Recent Advances in Electrocatalysts for Oxygen Reduction Reaction. *Chem. Rev.* **2016**, *116*, 3594–3657. [CrossRef] [PubMed]
4. Antolini, E. Palladium in fuel cell catalysis. *Energy Environ. Sci.* **2009**, *2*, 915–931. [CrossRef]
5. Stephen, A.J.; Rees, N.V.; Mikheenko, I.; Macaskie, L.E. Platinum and palladium bio-synthesized nanoparticles as sustainable fuel cell catalysts. *Front. Energy Res.* **2019**, *7*, 66. [CrossRef]
6. Esparza, R.; Santoveña, A.; Ruíz-Baltazar, A.; Angeles-Pascual, A.; Bahena, D.; Maya-Cornejo, J.; Ledesma-García, J.; Pérez, R. Study of PtPd bimetallic nanoparticles for fuel cell applications. *Mater. Res.* **2017**, *20*, 1193–1200. [CrossRef]
7. Kumar, S.S.; Himabindu, V. Hydrogen production by PEM water electrolysis—A review. *Mater. Sci. Energy Technol.* **2019**, *2*, 442–454. [CrossRef]
8. Zielińska-Jurek, A.; Hupka, J. Preparation and characterization of Pt/Pd-modified titanium dioxide nanoparticles for visible light irradiation. *Catal. Today* **2014**, *230*, 181–187. [CrossRef]
9. Baca, M.; Cendrowski, K.; Kukulka, W.; Bazarko, G.; Moszyński, D.; Michalkiewicz, B.; Kalenczuk, R.J.; Zielinska, B. A comparison of hydrogen storage in Pt, Pd and Pt/Pd alloys loaded disordered mesoporous hollow carbon spheres. *Nanomaterials* **2018**, *8*, 639. [CrossRef] [PubMed]
10. Geng, Z.; Wang, D.; Zhang, C.; Zhou, X.; Xin, H.; Liu, X.; Cai, M. Spillover enhanced hydrogen uptake of Pt/Pd doped corncob-derived activated carbon with ultra-high surface area at high pressure. *Int. J. Hydrogen Energy* **2014**, *39*, 13643–13649. [CrossRef]
11. Craig, B.; Anderson, D. *Handbook of Corrosion*; ASM International: Almere, The Netherlands, 1972.
12. Dhand, C.; Dwivedi, N.; Loh, X.J.; Ying, A.N.J.; Verma, N.K.; Beuerman, R.W.; Lakshminarayanan, R.; Ramakrishna, S. Methods and strategies for the synthesis of diverse nanoparticles and their applications: A comprehensive overview. *RSC Adv.* **2015**, *5*, 105003–105037. [CrossRef]
13. Yang, Y.; Cao, Y.; Yang, L.; Huang, Z.; Long, N.V. Synthesis of Pt–Pd bimetallic porous nanostructures as electrocatalysts for the methanol oxidation reaction. *Nanomaterials* **2018**, *8*, 208. [CrossRef] [PubMed]
14. You, G.; Jiang, J.; Li, M.; Li, L.; Tang, D.; Zhang, J.; Zeng, X.C.; He, R. PtPd(111) Surface versus PtAu(111) Surface: Which One Is More Active for Methanol Oxidation? *ACS Catal.* **2018**, *8*, 132–143. [CrossRef]
15. Zhang, X.; Guan, P.; Malic, L.; Trudeau, M.; Rosei, F.; Veres, T. Nanoporous twinned PtPd with highly catalytic activity and stability. *J. Mater. Chem. Mater.* **2015**, *3*, 2050–2056. [CrossRef]
16. Kim, J.; Jang, J.S.; Peck, D.H.; Lee, B.; Yoon, S.H.; Jung, D.H. Methanol-tolerant platinum-palladium catalyst supported on nitrogen-doped carbon Nanofiber for high concentration direct methanol fuel cells. *Nanomaterials* **2016**, *6*, 148. [CrossRef]
17. Lopes, T.; Antolini, E.; Gonzalez, E.R. Carbon supported Pt-Pd alloy as an ethanol tolerant oxygen reduction electrocatalyst for direct ethanol fuel cells. *Int. J. Hydrogen Energy* **2008**, *33*, 5563–5570. [CrossRef]
18. Li, H.; Sun, G.; Li, N.; Sun, S.; Su, D.; Xin, Q. Design and preparation of highly active Pt-Pd/C catalyst for the oxygen reduction reaction. *J. Phys. Chem.* **2007**, *111*, 5605–5617. [CrossRef]
19. Limpattayanate, S.; Hunsom, M. ORR Activity and Stability of Pt-Based Electrocatalysts in PEM Fuel Cell. *Int. J. Chem. Mol. Eng.* **2015**, *9*, 647–657.
20. Peng, Z.; Wu, J.; Yang, H. Synthesis and oxygen reduction electrocatalytic property of platinum hollow and platinum-on-silver nanoparticles. *Chem. Mater.* **2010**, *22*, 1098–1106. [CrossRef]
21. Termpornvithit, C.; Chewasatn, N. Hunsom, Stability of Pt-Co/C and Pt-Pd/C based oxygen reduction reaction electrocatalysts prepared at a low temperature by a combined impregnation and seeding process in PEM fuel cells. *J. Appl. Electrochem.* **2012**, *42*, 169–178. [CrossRef]
22. Quan, Z.; Wang, Y.; Fang, J. High-index faceted noble metal nanocrystals. *Acc. Chem. Res.* **2013**, *46*, 191–202. [CrossRef] [PubMed]

23. Ding, Y.; Gao, Y.; Wang, Z.L.; Tian, N.; Zhou, Z.Y.; Sun, S.G. Facets and surface relaxation of tetrahexahedral platinum nanocrystals. *Appl. Phys. Lett.* **2007**, *91*, 121901. [CrossRef]
24. Huang, X.; Zhao, Z.; Fan, J.; Tan, Y.; Zheng, N. Amine-assisted synthesis of concave polyhedral platinum nanocrystals having {411} high-index facets. *J. Am. Chem. Soc.* **2011**, *133*, 4718–4721. [CrossRef] [PubMed]
25. Tian, N.; Zhou, Z.Y.; Yu, N.F.; Wang, L.Y.; Sun, S.G. Direct electrodeposition of tetrahexahedral Pd nanocrystals with high-index facets and high catalytic activity for ethanol electrooxidation. *J. Am. Chem. Soc.* **2010**, *132*, 7580–7581. [CrossRef] [PubMed]
26. Rivera-Lugo, Y.Y.; Pérez-Muñoz, K.I.; Trujillo-Navarrete, B.; Silva-Carrillo, C.; Reynoso-Soto, E.A.; Yañez, J.C.C.; Lin, S.W.; Flores-Hernández, J.R.; Félix-Navarro, R.M. PTPD hybrid composite catalysts as cathodes for proton exchange membrane fuel cells. *Energies* **2020**, *13*, 316. [CrossRef]
27. Li, Z.; Deng, X.; Zhou, H.; Xuan, W.; Xie, Z.; Liu, F. Preparation of self-nitrogen-doped porous carbon nanofibers and their supported PtPd alloy catalysts for oxygen reduction reaction. *J. Solid State Electrochem.* **2020**, *24*, 195–206. [CrossRef]
28. Arias-Pinedo, O.M.; Riojas, A.A.C.; Pastor, E.; López, E.O.; Perez, G.; Archanjo, B.S.; Ponce-Vargas, M.; Planes, G.Á.; Baena-Moncada, A.M. Hierarchical Porous Carbon-PtPd Catalysts and Their Activity toward Oxygen Reduction Reaction. *ACS Omega* **2022**, *7*, 20860–20871. [CrossRef] [PubMed]
29. Zhang, X.; Wang, J.; Zhao, Y. Enhancement Mechanism of Pt/Pd-Based Catalysts for Oxygen Reduction Reaction. *Nanomaterials* **2023**, *13*, 1275. [CrossRef] [PubMed]
30. Ma, G.; Zhao, X.; Wang, J.; Qin, G.; Lu, Z.; Yu, X.; Li, L.; Zhang, X.; Yang, X. The Alloying Effect of PtPd/rGO and the Improvement of Its ORR Performance. *Catal. Lett.* **2024**, *154*, 2162–2170. [CrossRef]
31. Guterman, V.; Alekseenko, A.; Belenov, S.; Menshikov, V.; Moguchikh, E.; Novomlinskaya, I.; Paperzh, K.; Pankov, I. Exploring the Potential of Bimetallic PtPd/C Cathode Catalysts to Enhance the Performance of PEM Fuel Cells. *Nanomaterials* **2024**, *14*, 1672. [CrossRef] [PubMed]
32. Jelinek, B.; Groh, S.; Horstemeyer, M.F.; Houze, J.; Kim, S.G.; Wagner, G.J.; Moitra, A.; Baskes, M.I. Modified embedded atom method potential for Al, Si, Mg, Cu, and Fe alloys. *Phys. Rev. Condens. Matter. Mater. Phys.* **2012**, *85*, 245102. [CrossRef]
33. Thompson, A.P.; Aktulga, H.M.; Berger, R.; Bolintineanu, D.S.; Brown, W.M.; Crozier, P.S.; in't Veld, P.J.; Kohlmeyer, A.; Moore, S.G.; Nguyen, T.D.; et al. LAMMPS—A flexible simulation tool for particle-based materials modeling at the atomic, meso, and continuum scales. *Comput. Phys. Commun.* **2022**, *271*, 10817. [CrossRef]
34. Batyrev, I.G.; Coleman, S.P.; Ciezak-Jenkins, J.A.; Stavrou, E.; Zaug, J.M. Modeling and measurements of the XRD patterns of extended solids under high-pressure. *AIP Conf. Proc.* **2018**, *1979*, 050003. [CrossRef]
35. Raykhtsaum, G. Platinum alloys: A selective review of the available literature. *Platin. Met. Rev.* **2013**, *57*, 202–213. [CrossRef]
36. Massen, C.; Mortimer-Jones, T.V.; Johnston, R.L. Geometries and segregation properties of platinum-palladium nanoalloy clusters. *J. Chem. Soc. Dalton Trans.* **2002**, *23*, 4375–4388. [CrossRef]
37. Luyten, J.; De Keyzer, J.; Wollants, P.; Creemers, C. Construction of modified embedded atom method potentials for the study of the bulk phase behaviour in binary Pt-Rh, Pt-Pd, Pd-Rh and ternary Pt-Pd-Rh alloys. *Calphad* **2009**, *33*, 370–376. [CrossRef]
38. Aref'eva, L.P.; Dolgachev, Y.V. Phase diagram of nanoparticles of palladium-platinum alloys. *IOP Conf. Ser. Mater. Sci. Eng.* **2021**, *1029*, 012058. [CrossRef]
39. Goff, J.M.; Li, B.Y.; Sinnott, S.B.; Dabo, I. Quantifying multipoint ordering in alloys. *Phys. Rev.* **2021**, *104*, 054109. [CrossRef]
40. Zhang, L.; Roling, L.T.; Wang, X.; Vara, M.; Chi, M.; Liu, J.; Choi, S.; Park, J.; Herron, J.A.; Xie, Z. Platinum-based nanocages with subnanometer-thick walls and well-defined, controllable facets. *Science* **2015**, *349*, 412–416. [CrossRef] [PubMed]
41. Stukowski, A. Visualization and analysis of atomistic simulation data with OVITO-the Open Visualization Tool. *Model. Simul. Mat. Sci. Eng.* **2010**, *18*, 015012. [CrossRef]
42. Plimpton, S. Fast Parallel Algorithms for Short-Range Molecular Dynamics. *J. Comput. Phys.* **1995**, *117*, 1–19. [CrossRef]
43. Coleman, S.P.; Spearot, D.E.; Capolungo, L. Virtual diffraction analysis of Ni [0 1 0] symmetric tilt grain boundaries. *Model. Simul. Mat. Sci. Eng.* **2013**, *21*, 055020. [CrossRef]
44. Interatomic Potentials Repository. Available online: www.ctcms.nist.gov/potentials (accessed on 29 November 2024).
45. Zhou, X.W.; Johnson, R.A.; Wadley, H.N.G. Misfit-energy-increasing dislocations in vapor-deposited CoFe/NiFe multilayers. *Phys. Rev.* **2004**, *69*, 144113. [CrossRef]
46. Samsonov, V.M.; Romanov, A.A.; Kartoshkin, A.Y.; Talyzin, I.V.; Puytov, V.V. Embedding functions for Pt and Pd: Recalculation and verification on properties of bulk phases, Pt, Pd, and Pt–Pd nanoparticles. *Appl. Phys.* **2022**, *128*, 826. [CrossRef]
47. Samsonov, V.; Romanov, A.; Talyzin, I.; Lutsay, A.; Zhigunov, D.; Puytov, V. Puzzles of Surface Segregation in Binary Pt–Pd Nanoparticles: Molecular Dynamics and Thermodynamic Simulations. *Metals* **2023**, *13*, 1269. [CrossRef]
48. Chaisubanan, N.; Maniwan, W.; Hunsom, M. Effect of heat-treatment on the performance of PtM/C (M = Cr, Pd, Co) catalysts towards the oxygen reduction reaction in PEM fuel cell. *Energy* **2017**, *127*, 454–461. [CrossRef]

49. Bezerra, C.W.B.; Zhang, L.; Liu, H.; Lee, K.; Marques, A.L.B.; Marques, E.P.; Wang, H.; Zhang, J. A review of heat-treatment effects on activity and stability of PEM fuel cell catalysts for oxygen reduction reaction. *J. Power Sources* **2007**, *173*, 891–908. [CrossRef]
50. Chepkasov, I.V.; Gafner, Y.Y.; Vysotin, M.A.; Redel', L.V. A study of melting of various types of Pt–Pd nanoparticles. *Phys. Solid State* **2017**, *59*, 2076–2081. [CrossRef]
51. Deng, H.; Hu, W.; Shu, X.; Zhao, L.; Zhang, B. Monte Carlo Simulation of the Surface Segregation of Pt-Pd and Pt-Ir Alloys with an Analytic Embedded-Atom Method. *Surf. Sci.* **2002**, *517*, 177–185. [CrossRef]
52. Bernardi, F.; Alves, M.C.M.; Traverse, A.; Silva, D.O.; Scheeren, C.W.; Dupont, J.; Morais, J. Monitoring atomic rearrangement in PtxPd1-x (x) 1, 0.7, or 0.5) nanoparticles driven by reduction and sulfidation processes. *J. Phys. Chem.* **2009**, *113*, 3909–3916. [CrossRef]
53. An, W.; Liu, P. Size and shape effects of Pd@Pt core-shell nanoparticles: Unique role of surface contraction and local structural flexibility. *J. Phys. Chem.* **2013**, *117*, 16144–16149. [CrossRef]
54. Methfessel, M.; Hennig, D.; Scheffler, M. Trends of the surface relaxations, surface energies, and work functions of the 4d transition metals. *Phys. Rev.* **1992**, *46*, 8. [CrossRef]
55. Wang, L.L.; Johnson, D.D. Predicted trends of core-shell preferences for 132 late transition-metal binary-alloy nanoparticles. *J. Am. Chem. Soc.* **2009**, *131*, 14023–14029. [CrossRef] [PubMed]
56. De Clercq, A.; Giorgio, S.; Mottet, C. Pd surface and Pt subsurface segregation in Pt1−cPdc nanoalloys. *J. Phys. Condens. Matter.* **2016**, *28*, 064006. [CrossRef] [PubMed]
57. Nafday, D.; Sarkar, S.; Ayyub, P.; Saha-Dasgupta, T. A Reduction in Particle Size Generally Causes Body-Centered-Cubic Metals to Expand but Face-Centered-Cubic Metals to Contract. *ACS Nano* **2018**, *12*, 7246–7252. [CrossRef] [PubMed]
58. Wasserman, H.J.; Vermaak, J.S. On the determination of the surface stress of copper and platinum. *Surf. Sci.* **1972**, *32*, 168–174. [CrossRef]
59. Lamber, R.; Wetjen, S.; Jaeger, N.I. Size dependence of the lattice parameter of small palladium particles. *Phys. Rev.* **1995**, *51*, 10968–10971. [CrossRef]
60. Zhou, Z.Y.; Tian, N.; Li, J.T.; Broadwell, I.; Sun, S.G. Nanomaterials of high surface energy with exceptional properties in catalysis and energy storage. *Chem. Soc. Rev.* **2011**, *40*, 4167–4185. [CrossRef]
61. Zhuang, H.; Tkalych, A.J.; Carter, E.A. Surface Energy as a Descriptor of Catalytic Activity. *J. Phys. Chem.* **2016**, *120*, 23698–23706. [CrossRef]
62. Wen, Y.N.; Zhang, J.M. Surface energy calculation of the fcc metals by using the MAEAM. *Solid State Commun.* **2007**, *144*, 163–167. [CrossRef]
63. Mariscal, M.M.; Oldani, N.A.; Dassie, S.A.; Leiva, E.P.M. Atomistic computer simulations on the generation of bimetallic nanoparticles. *Faraday Discuss.* **2008**, *138*, 89–104. [CrossRef] [PubMed]
64. Ferrer, D.; Torres-Castro, A.; Gao, X.; Sepúlveda-Guzmán, S.; Ortiz-Méndez, U.; José-Yacamán, M. Three-layer core/shell structure in Au-Pd bimetallic nanoparticles. *Nano Lett.* **2007**, *7*, 1701–1705. [CrossRef] [PubMed]
65. Cheng, D.; Wang, W. Tailoring of Pd-Pt bimetallic clusters with high stability for oxygen reduction reaction. *Nanoscale* **2012**, *4*, 2408–2415. [CrossRef] [PubMed]
66. Mavrikakis, M.; Hammer, B.; Nørskov, J.K. Effect of strain on the reactivity of metal surfaces. *Phys. Rev. Lett.* **1998**, *81*, 2819–2822. [CrossRef]
67. Yang, X.; Wang, Y.; Tong, X.; Yang, N. Strain Engineering in Electrocatalysts: Fundamentals, Progress, and Perspectives. *Adv. Energy Mater.* **2022**, *12*, 2102261. [CrossRef]
68. Stamenkovic, V.; Mun, B.S.; Mayrhofer, K.J.J.; Ross, P.N.; Markovic, N.M.; Rossmeisl, J.; Greeley, J.; Nørskov, J.K. Changing the Activity of Electrocatalysts for Oxygen Reduction by Tuning the Surface Electronic Structure. *Angew. Chem.* **2006**, *118*, 2963–2967. [CrossRef]
69. Wang, W.; Wang, Z.; Wang, J.; Zhong, C.J.; Liu, C.J. Highly Active and Stable Pt–Pd Alloy Catalysts Synthesized by Room-Temperature Electron Reduction for Oxygen Reduction Reaction. *Adv. Sci.* **2017**, *4*, 1600486. [CrossRef]
70. Ali, S.; Myasnichenko, V.S.; Neyts, E.C. Size-dependent strain and surface energies of gold nanoclusters. *Phys. Chem. Chem. Phys.* **2015**, *18*, 792–800. [CrossRef]
71. Haouas, H.; El Atouani, L.; Sbiaai, K.; Hasnaoui, A. Size and temperature effects on surface energy of Au and Fe nanoparticles from atomistic simulations. *Comput. Mater. Sci.* **2022**, *214*, 111695. [CrossRef]
72. Long, N.V.; Ohtaki, M.; Hien, T.D.; Randy, J.; Nogami, M. A comparative study of Pt and Pt-Pd core-shell nanocatalysts. *Electrochim. Acta* **2011**, *56*, 9133–9143. [CrossRef]

73. Tao, F.; Grass, M.E.; Zhang, Y.; Butcher, D.R.; Renzas, J.R.; Liu, Z.; Chung, J.Y.; Mun, B.S.; Salmeron, M.; Somorjai, G.A. Reaction-driven restructuring of Rh-Pd and Pt-Pd core-shell nanoparticles. *Science* **2008**, *322*, 932–934. [CrossRef]
74. Bernardi, F.; Fecher, G.H.; Alves, M.C.M.; Morais, J. Unraveling the formation of core-shell structures in nanoparticles by S-XPS. *J. Phys. Chem. Lett.* **2010**, *1*, 912–917. [CrossRef]